



Reflective-Type Microring Resonator for On-Chip Reconfigurable Microwave Photonic Systems

Shilong Pan , Senior Member, IEEE, Zhenzhou Tang , Student Member, IEEE, Menghao Huang, and Simin Li, Member, IEEE

(Invited Paper)

Abstract—Microring resonator (MRR) is regarded as one of the most widely-used building blocks in photonic integration, which is employed to implement optical filtering, routing, sensing, true time delay, signal processing, logic operations and so on. However, a single MRR intrinsically produces Lorentzian or Lorentzian-derivative shape responses with very sharp peaks, which is incapable of handling wideband signals for microwave photonic systems. In this paper, we introduce a reflective-type MRR with a reflector connected to the drop port of an add-drop MRR. Thanks to the reflector, reconfigurable intensity and group delay responses can be achieved by setting the coupling coefficients of the MRR, leading to the implementation of flat-top filtering, wideband optical true time delay, XNOR/XOR optical logic operation and electro-optic modulation. Both theoretical analysis and experimental demonstration are carried out. This new MRR structure may enable a new, compact and low-cost design strategy for the integrated reconfigurable or programmable microwave photonic systems.

Index Terms—Ring resonator, silicon photonics, microwave photonics, optical filter, true time delay.

I. INTRODUCTION

MICRORING resonator (MRR) is regarded as one of the basic building blocks in photonic integrated circuits due to its capability of high efficient manipulation of optical signals with an unprecedented small footprint [1]–[8]. Fig. 1 shows two generic structures of the MRR, i.e., all-pass and add-drop ring resonators. The structure of the all-pass ring resonator is shown in Fig. 1(a), which consists of a straight bus waveguide and a looped waveguide. By designing the coupling between the bus and looped waveguides, the optical signal injected from the input port will be coupled into the ring resonator and looped back to the bus waveguide, resulting in multiple notches at the resonant wavelengths in the transmission response. Fig. 1(b) illustrated

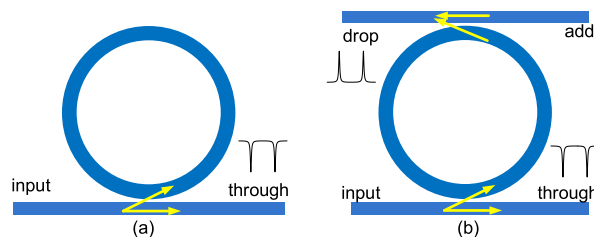


Fig. 1. Generic structures of the MRRs for photonic integrated circuits. (a) The all-pass MRR and (b) the add-drop MRR.

the structure of the add-drop ring resonator, which is a four-port device with two bus waveguides and a looped waveguide. By adjusting the two coupling regimes, multiple transmission peaks at the resonant wavelengths will be observed at the drop port, in addition to the notches at the through port. Based on the MRR, a lot of applications can be realized, including add-drop multiplexing [9], optical buffering [10], optical sensing [11]–[13], optical logic gate [14], lasing [15], electrooptic modulation [16], [17], optical delay [18], [19], on-chip optical frequency comb generation [20]–[22], soliton-based microwave synthesis [23], [24] and so on.

However, a single MRR intrinsically produces a Lorentzian magnitude response with a very sharp peaks (or notches), leading to a narrow signal handling bandwidth. To solve this problem, a number of MRRs connected in series or parallel are usually required. For example, in [25], three parallel add-drop MRRs were used to realize a flat-top optical filter with 0.38-nm bandwidth and 40-dB out-of-band rejection. J. R. Ong *et al.* inserted five ring resonators between two bus waveguides to produce an optical filter with a tunable bandwidth within 12 to 125 GHz and an out-of-band rejection ratio of 100 dB [26]. To realize large on-chip optical delay, a photonic integrated circuit incorporating as many as 40 MRRs was reported [27], which achieved a time delay of 535 ps for 20-GHz signals and 632 ps for 10-GHz signals. The main problems associated with the use of multiple MRRs are the significant increase of the chip footprint, the insertion loss, the transmission latency, and the difficulty of fabrication. In addition, a large number of controllers and feedback circuits should be applied to precisely adjust the coupling coefficients and radii of the MRRs so that the central wavelengths of the MRRs can be aligned to synthesize a broad

Manuscript received December 1, 2019; revised January 9, 2020; accepted January 10, 2020. Date of publication January 30, 2020; date of current version February 7, 2020. This work was supported in part by the National Natural Science Foundation of China under Grants 61527820 and 61604072 and in part by the Fundamental Research Funds for the Central Universities. (Corresponding authors: Shilong Pan; Zhenzhou Tang.)

The authors are with the Key Laboratory of Radar Imaging and Microwave Photonics, Ministry of Education, Nanjing University of Aeronautics and Astronautics, Nanjing 210016, China (e-mail: pans@iee.org; tangzhzh@nuaa.edu.cn; hmh19880525@163.com; lisimin@nuaa.edu.cn).

Color versions of one or more of the figures in this article are available online at <https://ieeexplore.ieee.org>.

Digital Object Identifier 10.1109/JSTQE.2020.2969567

bandwidth. Moreover, a conventional MRR can only achieve either band-stop response at the through port or bandpass response at the drop port. A switch between the two kinds of responses for a given port is impossible, which provides a very limited reconfigurability. Therefore, although the conventional MRRs have very simple structures, they may encounter difficulties for large-scale, low-cost, and wideband on-chip reconfigurable or programmable microwave photonic systems.

To overcome this problem, the freedom of reflection can be used [28]. Previously, we have proposed a novel reflective-type MRR which enables broadband signal processing capability and high reconfigurability of the ring resonator [29], [30]. The reflective-type MRR consists of an add-drop ring resonator and an on-chip reflector connected to the drop port of the resonator, so the optical signal at the drop port will be reflected back to the looped waveguide. By this way, the lightwave will propagate along the two opposite directions in the common ring cavity, which stimulates the bandpass (slow light) and band-stop (fast or slow light, depending on the coupling coefficients) intensity or group delay responses, respectively. By adjusting the coupling coefficients of the MRR, the strengths of the bandpass (slow light) and band-stop (fast or slow light) responses can be independently adjusted. Combining the two responses at the output port of the reflective MRR (i.e., the add port of the add-drop ring resonator), a reconfigurable intensity (group delay) response can be obtained. Compared to traditional cascaded MRRs [25]–[27], the reflective-type MRR re-uses the same MRR for a two-stage filter, which reduces the chip footprint, the number of heater controllers and also enables a more stable on-chip system. Some preliminary observation of the reflective-type MRR was reported [29] and a theoretical analysis was performed [30].

In this paper, comprehensive theoretical and experimental investigation of the new MRR structure is carried out. The application of the reflective-type MRR to establish a reconfigurable microwave photonic system with the capabilities of flat-top optical filtering, flat-top optical true time delay, optical XNOR/NOR logics and electro-optic modulation is experimentally demonstrated.

The paper is organized as follows. In Section II, the structure, principle and fabrication of the reflective-type MRR is introduced. Section III presents the simulation and experiment results of the reconfigurable microwave photonic system, including flat-top optical filtering, optical true time delay and its application in multi-beam phased array antennas, optical XNOR/NOR logic and thermo-optic modulation. Finally, discussions and conclusions are presented in Section IV.

II. PRINCIPLE AND DEVICE

Fig. 2 shows the structure of the reflective-type MRR, which can be simply viewed as a conventional add-drop MRR with a reflector connected to the drop port. The reflector could be a Bragg grating, a loop mirror and so on. When an optical signal is injected into the ring resonator through Port_1, it is coupled into the looped waveguide and transmitted to Port_3 along the counterclockwise (CCW) direction. Based on the transfer matrix formalism, the intensity transmission response when the

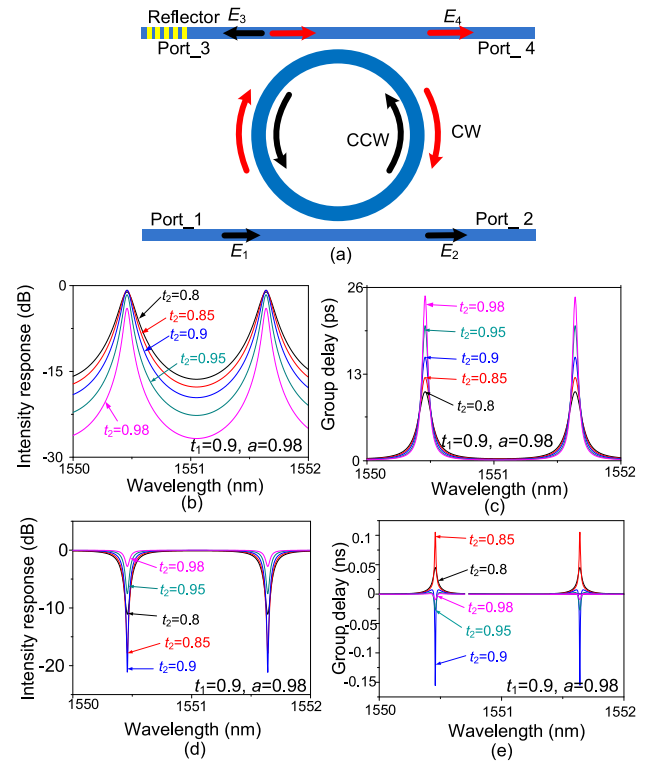


Fig. 2. The structure of the reflective-type MRR and the calculated transmission responses for different propagation directions. (a) The configuration of the reflective-type MRR, (b) the intensity and (c) group delay responses when the lightwave transmits from Port_1 to Port_3, and (d) the intensity and (e) group delay responses when the reflected lightwave propagates from Port_3 to Port_4.

lightwave goes from Port_1 to Port_3 can be written as

$$T_{31} = \frac{(1 - t_1^2)(1 - t_2^2)a}{1 - 2t_1t_2a \cos \phi + (t_1t_2a)^2} \quad (1)$$

where a is the single-pass transmission coefficient related to the power attenuation coefficient of the waveguide, $\phi = \beta L$ is the single-pass optical phase shift determined by both the propagation constant of the circulating mode (β) and the length of the looped waveguide (L), t_1 and t_2 are the amplitude self-coupling coefficients at the lower and upper coupling sections. When a is fixed at 0.98, t_1 is fixed at 0.9, t_2 is adjusted from 0.8 to 0.98, the calculated intensity responses are shown in Fig. 2(b). Lorentzian-shaped lines with periodical peaks are observed, which can be considered as a bandpass optical filter with multiple passbands. Besides, when increasing t_2 to make the MRR approach the critical coupling state, the extinction ratio together with the quality factor is greatly increased, and the insertion loss is decreased, since most of the light will be coupled into the looped waveguide. The corresponding group delay response can be expressed as [30]

$$\tau_{31} = \left(\frac{1}{2} + \frac{at_1t_2 \cos \phi - (t_1t_2a)^2}{1 - 2t_1t_2a \cos \phi + (t_1t_2a)^2} \right) \frac{n_g L}{c} \quad (2)$$

where n_g is the group refractive index and c is the light speed in vacuum. If the wavelength of the input optical signal is around one of the resonant wavelengths of the ring resonator, i.e.,

$\cos\phi \approx 1$, (2) can be simplified to

$$\tau_{31} \approx \frac{1 + t_1 t_2 a}{2(1 - t_1 t_2 a)} \frac{n_g L}{c} \quad (3)$$

The calculated group delay response is shown in Fig. 2(c), in which n_g is set to be 1.71 and L is set to be $200\pi \mu\text{m}$. Obviously, the group delay is always positive, indicating that the slow-light effect presents when the lightwave propagates from Port_1 to Port_3. Moreover, the group delay increases with t_2 .

When a reflector is placed at Port_3, the lightwave is partly or entirely reflected and re-coupled into the looped waveguide along the clockwise (CW) direction. If all the lightwave is reflected at Port_3, and transmitted to Port_4, the intensity response can be written as

$$T_{43} = \frac{a^2 t_1^2 - 2t_1 t_2 a \cos\phi + t_2^2}{1 - 2t_1 t_2 a \cos\phi + (t_1 t_2 a)^2} \quad (4)$$

Again, the intensity response is calculated and illustrated in Fig. 1(d). Multiple notches are observed, which can be viewed as a band-stop optical filter with multiple notches. As shown in Fig. 1(d), when t_2 is increased from 0.8 (the over coupling state) to 0.9 (close to the critical coupling state), the depth of the notch is increased. If t_2 further increases, the notch depth goes down since the ring resonator is now operated at the under coupling state. The group delay response in this case is given by

$$\tau_{43} = \left(\frac{a^2 t_2^2 - a t_1 t_2 \cos\phi}{a^2 t_2^2 + t_1^2 - 2a t_1 t_2 \cos\phi} + \frac{a t_1 t_2 \cos\phi - a^2 t_1^2 t_2^2}{1 + a^2 t_1^2 t_2^2 - 2a t_1 t_2 \cos\phi} \right) \frac{n_g L}{c} \quad (5)$$

The calculated group delay is shown in Fig. 2(e). As can be seen, either positive or negative group delay can be obtained, depending on the coupling coefficient t_2 . Specifically, when the ring resonator is operated at the over coupling state (i.e., $t_2 = 0.8$ and 0.85), positive group delay is achieved, which indicates that slow-light effect is presented. On the other hand, when the ring resonator is operated at the under coupling state (i.e., $t_2 \geq 0.9$), negative group delay is observed due to the anomalous dispersion [31], indicating the presence of the fast-light effect. The largest negative group delay is obtained when $t_2 = 0.9$.

It should be noted that, if no reflector is put at Port_3, no light will propagate to Port_4. Besides, since the reflected light will not be transmitted to Port_2, the transmission response at Port_2 will keep unchanged.

From the above analysis, the reflective-type MRR can perform both bandpass (slow-light) and band-stop (fast- or slow-light) intensity or group delay responses in a single ring resonator, and the strengths of the two responses can be manipulated by changing the coupling coefficients of the MRR. Therefore, a new ring resonator with more flexibility and compactness is achieved, as compared with the conventional photonic integrated circuits based on multiple MRRs [25]–[27].

A low-loss (<0.5 dB/cm) silicon nitride platform (TriPleX [32]) is employed to fabricate such a reflective-type MRR. The structure and microscope image of the fabricated reflective-type MRR are shown in Fig. 3(a) and (b), respectively. The total

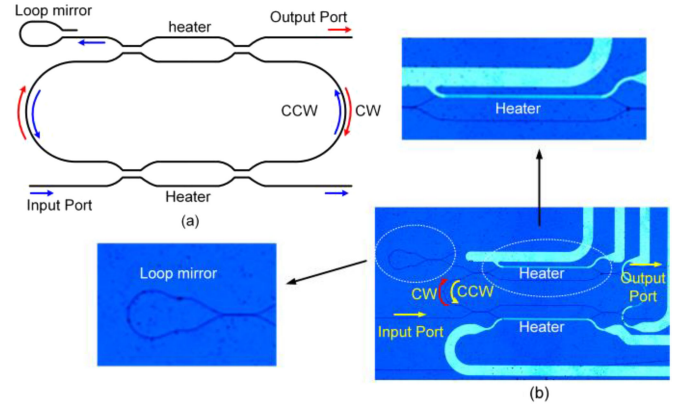


Fig. 3. (a) Structure and (b) microscope image of the fabricated reflective-type MRR. Insets: zoom-in views of the loop mirror and the asymmetric Mach-Zehnder interferometer with a thermo-optic heater.

length of the ring cavity is $4293.9 \mu\text{m}$ and the group index is ~ 1.71 , corresponding to a FSR of 0.3272 nm. To realize the on-chip optical reflection, a loop mirror consisting of an optical coupler and a looped waveguide (shown as the inset) is employed and connected to the drop port of the ring resonator. According to the principle of the loop mirror, the strength of the reflected light is related to the coupling ratio of the optical coupler in the loop mirror. In order to make the reflector work, the coupling length should be properly designed according to the resonant wavelength of the MRR. In our design, the coupling length of the optical coupler is designed to obtain a 50:50 coupling ratio, so the lightwave can be entirely reflected [33]. Besides, in order to adjust the coupling coefficients, two asymmetric Mach-Zehnder interferometers (AMZIs) with two thermo-optic heaters are employed, as presented in the inset of Fig. 3. The length of the thermo-optic heater is $800 \mu\text{m}$. It should be noted that the reflective-type MRR can be fabricated using any other optical substrate, such as lithium niobate film, silicon on insulator, polymer, and indium phosphide.

III. EXPERIMENT AND RESULTS

By using the reflective-type MRR, reconfigurable microwave photonic systems can be established, which can be used to realize flat-top optical and microwave filtering, optical true time delay, optical XNOR/NOR logic operation, and electro-optic modulation.

A. Flat-Top Optical and Microwave Filtering

Filtering is one of the basic and most important functionalities of optical or microwave systems, for wavelength or frequency selection, noise rejection and performance monitoring. In general, an MRR can easily realize optical filtering thanks to its intrinsic bandpass frequency response at the drop port or band-stop frequency response at the through port [34]. By inserting a single sideband (SSB) electro-optic modulator (EOM) or a phase modulator before the MRR and a photodetector (PD) after the MRR, the filtering function can be mapped into the microwave domain [35]–[37].

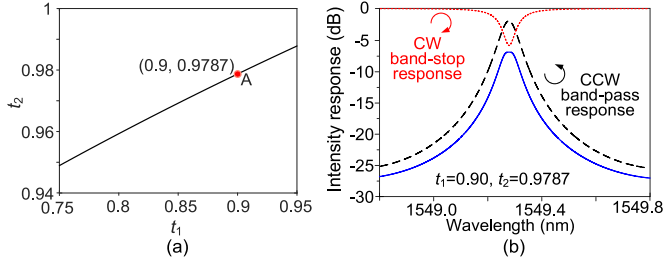


Fig. 4. (a) The relationship between t_1 and t_2 to obtain a flat-top optical filter and (b) the simulated intensity response when $t_1 = 0.9$ and $t_2 = 0.9787$. Red dashed line: CW band-stop response; black short-dashed line: CCW bandpass response.

One key challenge associated with the MRR-based filters is that the bandwidth is usually limited by the Lorentzian magnitude response. In addition, the conventional MRR can only achieve either band-stop response at the through port or bandpass response at the drop port, leading to very limited reconfigurability. By simply adding a reflector at the drop port of the ring resonator, both the bandpass and band-stop responses can be produced using a single ring resonator, and the strengths of the bandpass and band-stop responses can be tuned by adjusting the coupling coefficients, as can be seen from Fig. 2(b) and 2(d), so a reconfigurable (especially highly-desirable flat-top) optical or microwave filter can be implemented.

Mathematically, the intensity response when a lightwave propagates from Port_1 to Port_4 can be written as

$$T_{41} = \frac{t_1^2 a^2 - 2t_1 t_2 a \cos \phi + t_2^2 + (1 - t_1^2)(1 - t_2^2)a}{1 - 2t_1 t_2 a \cos \phi + (t_1 t_2 a)^2} \quad (6)$$

To realize a flat-top optical filter, $dT_{41}/d\cos\phi$ should be zero, leading to

$$\frac{dT_{41}}{d\cos\phi} = \frac{-2a^2 t_1 t_2 (1 - t_1^2) (1 - t_2^2)}{[1 + (at_1 t_2)^2 - 2a^2 t_1^2 - t_2^2 + 2at_1 t_2 \cos\phi]^3} = 0 \quad (7)$$

$$t_2 = \frac{1 + \sqrt{2}at_1}{\sqrt{2} + at_1} \text{ or } t_2 = \frac{\sqrt{2}at_1 - 1}{\sqrt{2} - at_1} \quad (8)$$

That is to say, when t_1 and t_2 satisfy the relationship in Eq. (8), flat-top optical filtering can be achieved. The former solution corresponds to the condition that the CW mode is operated at the under coupling state, and the latter one represents the case that the CW mode is operated at the over coupling state. Since the MRR in the under coupling state has a much higher quality factor, which is preferred for optical or microwave filtering, only the former case is considered in the following analysis. Fig. 4(a) plots the relationship between t_1 and t_2 , when $a = 0.98$, and Fig. 4(b) shows the simulated intensity response when $t_1 = 0.9$ and $t_2 = 0.9787$, corresponding to Point A on the curve in Fig. 4(a). The CCW bandpass response and the CW band-stop response are also plotted in Fig. 4(b). As can be seen, an optical filter with flat-top passband is obtained, which agrees well with

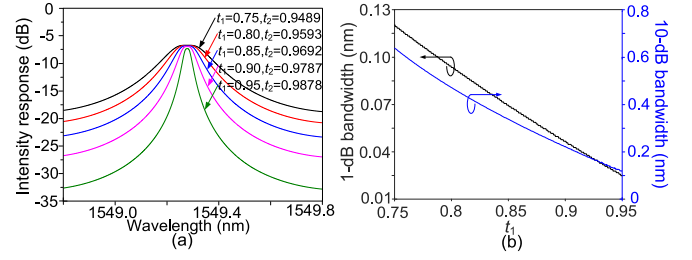


Fig. 5. The calculated flat-top optical filter responses with different bandwidths. (a) The intensity responses and (b) the 1- and 10-dB bandwidths with different t_1 .

the analytical analysis. It can be seen from Fig. 4(a) that the response of the optical filter is sensitive to the value of t_2 . To maintain t_2 , a low-ripple DC voltage source and feedback loop can be used. When adjusting t_1 and t_2 to other values, flat-top optical filters with different bandwidths can be realized, which are shown in Fig. 5(a). The loss of the optical filter is a bit higher due to the reduction of the CW band-stop response, which can be compensated by optical amplification. Although the loss is increased, the bandwidth of the optical filter is extended, compared with the conventional Lorentzian-shaped MRR. When t_1 and t_2 are increased, the optical bandwidth is reduced. Fig. 5(b) depicts the calculated 1-dB and 10-dB bandwidths with different t_1 (t_2 is correspondingly changed according to Eq. (8)). Nearly linear relationships can be observed, which means that the bandwidth of the flat-top optical filter can be flexibly adjusted by tuning the coupling coefficients of the reflective-type MRR. As can be seen from Fig. 5, when the bandwidth increases, the roll-off and stop-band attenuation of the optical filter decrease. This is because the well-known case that the MRR will deviate from the critical coupling condition when t_2 is reduced from 0.95 to 0.75, which leads to a reduced quality factor [6]. It should also be noted that we only analyze the flat-top condition in this paper. Actually, when t_1 and t_2 do not satisfy the relationship in Eq. (8), Lorentzian response or resonance split response will be produced at Port_4. A detailed analysis of these filter shapes realized by the reflective-type MRR can be found in our previous works [29], [30].

An optical vector analyzer [38]–[41] based on optical SSB modulation is employed to measure the magnitude and phase responses of the reflective-type MRR, with the measurement setup shown in Fig. 6(a). An optical laser source is sent to an electro-optic modulator (EOM), which is driven by a frequency-swept microwave source produced by an electrical vector network analyzer (EVNA). A tunable optical bandpass filter with a roll-off slope of 500 dB/nm (Yenista XTM-50) is followed to remove one of the two first-order sidebands to generate an optical SSB-modulated signal. The bandwidth of the optical filter is about 0.4 nm and the undesired sideband is suppressed by more than 40 dB. After being amplified by an erbium-doped fiber amplifier (EDFA), the optical SSB-modulated signal is injected into the reflective-type MRR through Port_1. The optical signal output from Port_4 is connected to a PD, and the generated electrical signal is sent back to the EVNA to perform magnitude and phase detections.

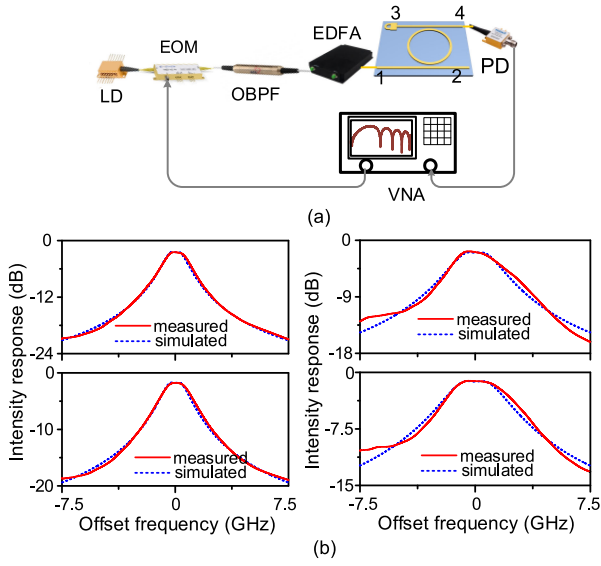


Fig. 6. (a) The measurement setup and (b) the measured results of the proposed reflective-type MRR when the coupling coefficients are adjusted.

Fig. 6(b) shows the unnormalized measurement results with the coupling losses excluded. As can be seen, by properly choosing the coupling coefficients of the reflective-type MRR, flat-top responses can be generated. More importantly, when adjusting the coupling coefficients, the bandwidths of the optical filters will be changed while the flat-top passbands are maintained. The calculated results are presented as the dashed line in Fig. 6(b). In our simulation, the transmission loss of the waveguide is 0.5 dB/cm, the cavity length is 4676.8 μm , the group index n_g is 1.71, and the combinations of t_1 and t_2 are (0.9374, 0.9848), (0.9277, 0.983), (0.8839, 0.975) and (0.8202, 0.9626). When comparing with the simulated results shown as the dashed line in Fig. 6(b), we can see that the measured results agree well with the simulation. With the similar setups in [35]–[37], flat-top microwave filters with good reconfigurability could be constructed. Similar to the calculated results shown in Fig. 5(a), the extinction ratio of the optical filter is reduced when the bandwidth increases, which is also owing to the deviation from the critical coupling condition. Besides, asymmetric frequency responses are observed when the bandwidth is increased, which might be due to the slightly unidentical propagation constants of the CW and CCW modes.

Fig. 7 also presents the measured frequency responses at Port_4 when t_1 is fixed and t_2 is tuned. When t_2 is tuned, the frequency response is changed from resonance split to flat-top, and finally becomes Lorentzian shape, which agrees with the results in our previous paper [29].

B. Optical True Time Delay

Optical true time delay based beamforming is regarded as a powerful solution for wideband phased array antennas (PAAs), since it can avoid the beam-squint problem compared with the conventional PAAs based on microwave phase shifters [42]. MRRs are widely adopted to implement the optical true time

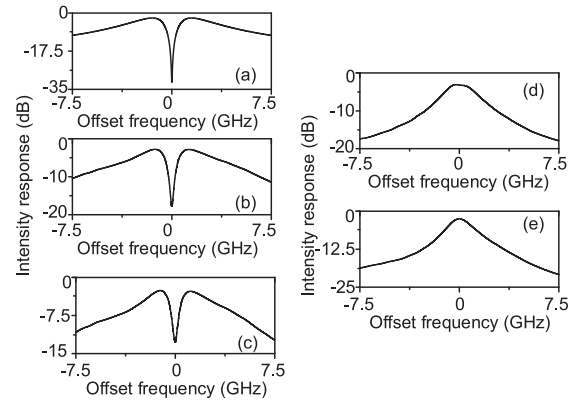


Fig. 7. (a)–(e) Measured frequency responses at Port_4 when t_1 is fixed and t_2 is tuned.

delays due to their small footprint, low loss and potentially high volume integration [19], [27], [43]. However, according to the well-known Kramers–Kronig relation, a single MRR can only achieve a time delay within a relatively small bandwidth. Again, by using the reflective-type MRR, the group-delay bandwidth can be dramatically increased [29], [30].

Mathematically, the group delay response of the reflective-type MRR is given by

$$\tau_{41} = \left(\frac{1}{2} + \frac{a^2 t_1^2 - a t_1 t_2 \cos \phi}{a^2 t_1^2 + t_2^2 - 2 a t_1 t_2 \cos \phi} + \frac{2 (a t_1 t_2 \cos \phi - a^2 t_1^2 t_2^2)}{1 + a^2 t_1^2 t_2^2 - 2 a t_1 t_2 \cos \phi} \right) \frac{n_g L}{c} \quad (9)$$

Similarly, to achieve a flat-top group delay response, $d\tau_{41}/d \cos \phi = 0$, i.e.,

$$\frac{d\tau_{41}}{d \cos \phi} = \left(\frac{a^3 t_1^3 t_2 - a t_1 t_2^3}{(a^2 t_1^2 + t_2^2 - 2 a t_1 t_2 \cos \phi)^2} + \frac{2 (a t_1 t_2 - a^3 t_1^3 t_2^3)}{(1 + a^2 t_1^2 t_2^2 - 2 a t_1 t_2 \cos \phi)^2} \right) \frac{n_g L}{c} = 0 \quad (10)$$

Applying the equation of $\cos \phi = 1$ (close to the resonant wavelengths) to Eq. (10), the solution can be written as

$$\frac{a t_1 + t_2}{1 + a t_1 t_2} = \frac{-2 (a t_1 - t_2)^3}{(1 - a t_1 t_2)^3} \quad (11)$$

According to the group delay responses shown in Figs. 2(c) and 2(e), we can predict that the flat-top group delay can only be obtained when a weak fast-light effect is introduced during the CW propagation, which means that $t_2 \approx 1$, thus Eq. (11) can be simplified to

$$\frac{a t_1 + t_2}{1 + a t_1 t_2} = \frac{-2 (a t_1 - t_2)^3}{(1 - a t_1 t_2)^3} \approx 1 \quad (12)$$

From Eq. (12), the relationship between t_1 and t_2 for the flat-top time delay response can be obtained, which is

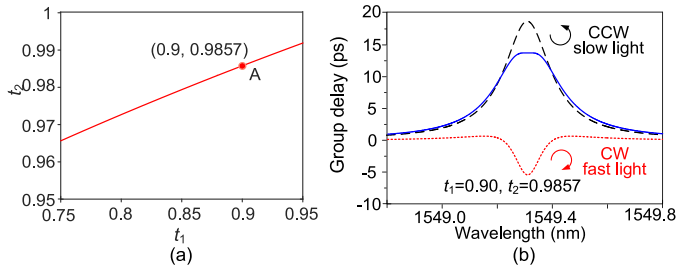


Fig. 8. (a) The calculated relationship between t_1 and t_2 to obtain a flat-top group delay and (b) the group delay response when $t_1 = 0.9$ and $t_2 = 0.9857$. Red dashed line: CW fast-light response; black short-dashed line: CCW slow-light response.

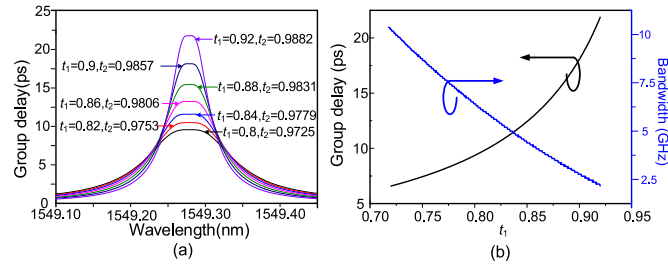


Fig. 9. The calculated flat-top group delay responses with different bandwidths. (a) The group delay responses, (b) the group delay and the 1-ps bandwidth with different t_1 .

given by

$$t_2 = \frac{1 + \sqrt[3]{2}at_1}{\sqrt[3]{2} + at_1} \text{ or } t_2 = \frac{\sqrt[3]{2}at_1 - 1}{\sqrt[3]{2} - at_1} \quad (13)$$

Similarly, only the former solution in Eq. (13) is analyzed. Fig. 8(a) plots the relationship between t_1 and t_2 according to Eq. (13). When t_1 is chosen to be 0.9, to achieve a flat-top group delay, t_2 should be 0.9857. The corresponding group delay response in this case is calculated and plotted in Fig. 8(b). As can be seen from the short-dashed line in Fig. 8(b), when the lightwave propagates from Port_1 to Port_3 along the CCW direction, the strong slow-light effect would produce a Lorentzian-like group delay response, as depicted as the black short-dashed line in Fig. 8(b). When the lightwave at Port_3 is reflected by the loop mirror and transmitted to Port_4 along the CW direction, a weak fast-light effect induced Lorentzian-shaped group delay response is obtained, as shown as the red dashed line in Fig. 8(b). As a result, a flat-top group delay response is achieved by combining both responses, as shown as the solid line.

The group delay responses associated with different t_1 and t_2 are plotted in Fig. 9(a). When t_1 (or t_2) is increased, flat-top group delay responses with increased group delays can be achieved. Meanwhile, the 1-ps bandwidth is decreased due to the increase of the quality factor of the MRR. Fig. 9(b) shows the calculated group delay and the 1-ps bandwidth with different t_1 . Although increasing the group delay will sacrifice the operational bandwidth, the reflective-type MRR still has a larger operational bandwidth than that based on the conventional MRR thanks to the flat-top group delay responses.

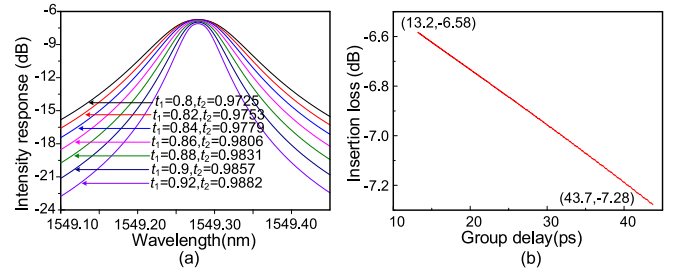


Fig. 10. The calculated intensity responses when the reflective-type MRR is used as a flat-top true time delay element. (a) The intensity responses and (b) the relationship between the passband insertion loss and the group delay.

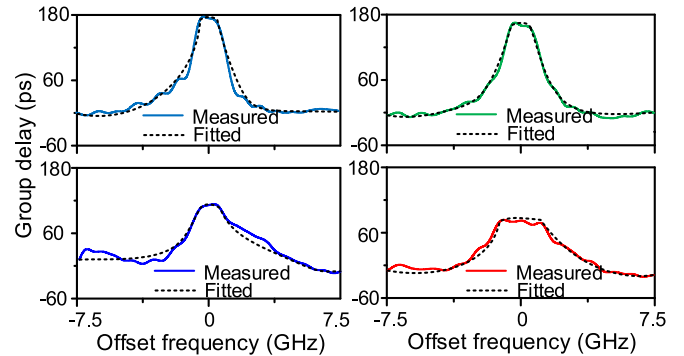


Fig. 11. Measured flat-top group delay responses with different group delays.

It should be noted that the conditions to achieve the flat-top group delay responses are slightly different from those for flat-top intensity responses. Fig. 10(a) shows the calculated intensity responses of the reflective-type MRR when it is functioned as a flat-top optical true time delay element. Compared with most of the conventional MRR-based true time delay elements that usually perform true time delay within lossy and band-stop responses [44], bandpass responses with small passband loss variation are observed, which is more attractive for the PAA applications to reduce the requirement of loss balance. Fig. 10(b) shows the insertion losses with different group delays. The calculated insertion loss variation is as low as 0.8 dB when the group delay is tuned from 13.2 to 43.7 ps.

Fig. 11 shows the group delay responses with different combinations of t_1 and t_2 , which are measured by the optical vector analyzer shown in Fig. 6(a). The measured group delay is 73, 110, 159 and 180 ps, respectively. The ripple in the passband might be resulted from the group delay measurement scheme, which is sensitive to the phase drift that cannot be neglected due to the vibration and temperature variation in the laboratory environment. Fig. 12 presents the measured insertion losses (with the coupling losses excluded) with different group delays. The insertion loss variation is lower than 0.8 dB within more than 100-ps group delay tuning range, which agrees well with the theoretical prediction, indicating that the reflective-type MRR based true time delay element is suitable for wideband reconfigurable photonic systems since it can save at least one on-chip attenuator and the corresponding control circuit [10].

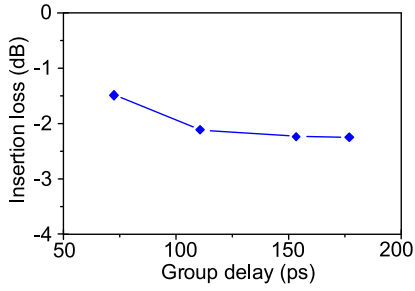


Fig. 12. Measured insertion loss (coupling loss excluded) versus the group delay.

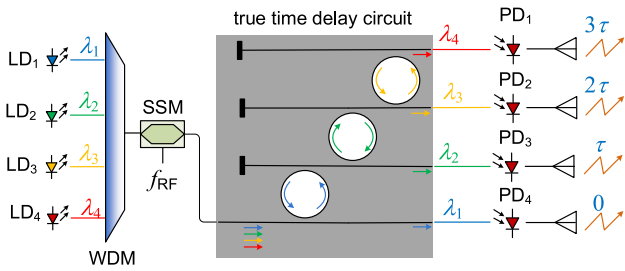


Fig. 13. A phased array antenna system based on the reflective-type MRRs.

Based on the optical true time delay element realized by the reflective-type MRR, PAAs can be established. Fig. 13 shows a typical one-dimensional PAA based on the reflective-type MRRs. In the system, four laser diodes (LDs) produces four optical carriers with different wavelengths, which are combined by a wavelength-division multiplexer (WDM) and sent to a single sideband modulator (SSM) driven by an RF signal. The modulated optical signal is applied to the integrated optical true time delay circuits based on multiple reflective-type MRRs. By properly designing the radii of the ring resonators, optical components with different wavelengths will pass through different MRRs. For example, λ_1 is located between two resonant wavelengths of the first reflective-type MRR, and λ_3 is aligned to one the resonant wavelengths of the first and second ring resonators but deviated from any resonant wavelengths of the third MRR. As a result, the four wavelengths undergo different time delays, as shown in Fig. 12. Thanks to the optical filtering nature of the MRRs, the input optical signals are separated according to their wavelengths. After the optical-to-electrical conversion in PDs, the generated electrical signals with different time delays are emitted to the free space through electrical antennas to realize far-field RF beamforming.

Figs. 14(a) to (c) show the intensity responses of the three reflective-type MRRs for the PAA system. The three ring resonators are designed to have free spectral ranges (FSRs) of 0.68, 0.544 and 0.408 nm, respectively. By properly choosing the wavelength of λ_1 , the signal can go directly to PD₄ without interacting with any ring resonator, so the time delay of this channel can be viewed as the reference. λ_2 is aligned to the third transmission peak of the first ring resonator and located between the third and fourth peaks of the second ring resonator, so it will only undergo one-trip time delay (τ_2), and output from PD₃.

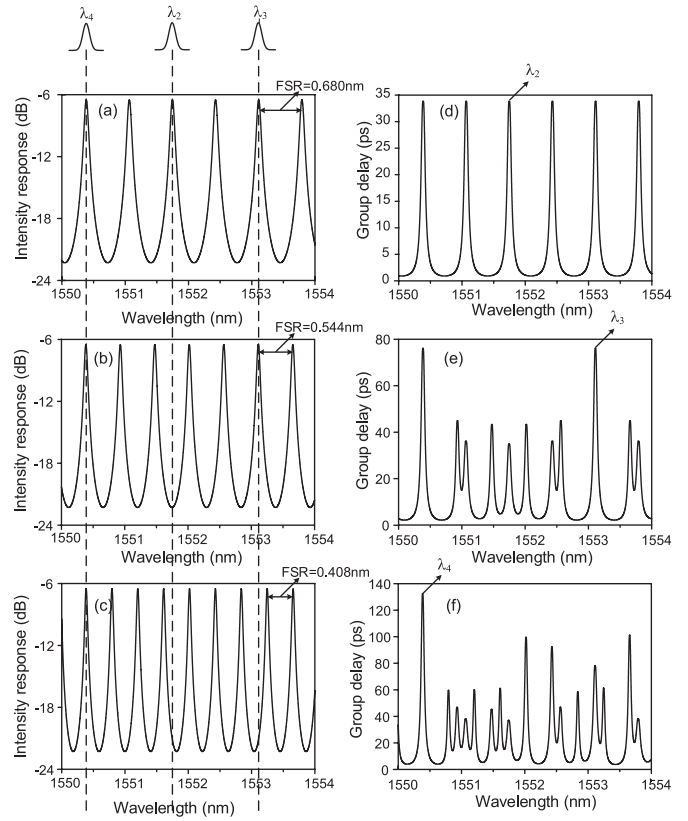


Fig. 14. (a)–(c) The calculated intensity responses of the three reflective-type MRRs for the PAA system, and the accumulated group delay responses for λ_2 , λ_3 , and λ_4 , respectively.

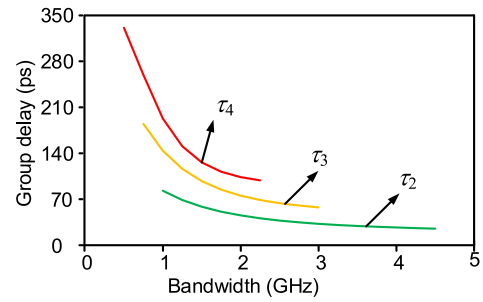


Fig. 15. Calculated time group delays in each channel versus the RF bandwidth.

The group delay response of this channel is shown in Fig. 14(d). Since λ_3 is aligned to the resonant wavelengths of the first and second ring resonators, the total delay (τ_3) is the sum of the group delays introduced by the two resonators, which can be seen from Fig. 14(e). λ_4 is chosen to match the passbands of all the three ring resonators, so the time delay (τ_4) is contributed by the group delays of all the three resonators, as illustrated in Fig. 14(f).

Fig. 15 shows the calculated group delays versus the RF bandwidths. For the λ_2 channel, τ_2 is decreased from 91.82 to 24.28 ps when the bandwidth is increased from 1 to 4.5 GHz; for the λ_3 channel, τ_3 is decreased from 204.59 to 54.78 ps when the bandwidth is increased from 0.75 to 3 GHz; and for

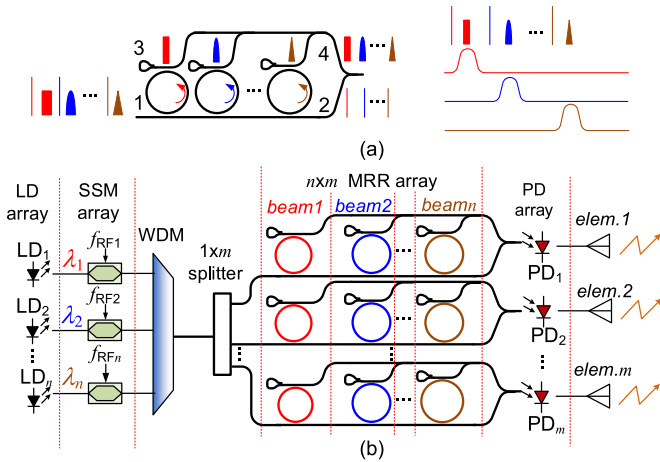


Fig. 16. (a) Reflective-type-MRR-based true time delay element for multi-beam PAAs, and (b) a $n \times m$ PAA system based on the reflective-type MRRs. SSM: single sideband modulator.

the λ_4 channel, τ_4 is decreased from 346.12 to 94.58 ps when the bandwidth is increased from 0.5 to 2.25 GHz. For a typical PAA system, time delays of the different channels usually satisfy $\tau_4 = 3\tau_2$, $\tau_3 = 2\tau_2$, so the time delay ranges of the PAA system shown in Fig. 12 can be: $\tau_2 \in [31.62, 91.82]$, $\tau_3 \in [63.24, 183.64]$ and $\tau_4 \in [94.85, 275.64]$.

The reflective-type MRRs can also be used to realize a multi-beam PAA. Fig. 16(a) shows a typical architecture of the true time delay element based on the reflective-type MRRs for multi-beam PAAs. Different RF signals are modulated onto different optical carriers by optical SSB modulation, and then injected into the cascaded MRRs through Port_1. By properly designing the reflective-type MRRs and carefully choosing the optical wavelengths, the optical carriers and the sidebands will be separated due to the optical filtering nature of the MRRs. The optical carriers will directly propagate to Port_2, and the sidebands will be coupled into different reflective-type MRRs and then reflected to Port_4. Each reflective-type MRR would introduce an independently-tunable optical time delay to the sideband circulating in it. When the optical carrier and the sidebands are re-combined and sent to a PD, multiple RF signals with different time delay are obtained. Based on this concept, an $n \times m$ PAA system can be constructed, as shown in Fig. 16(b). A LD array generates n optical carriers and modulated by multiple RF signals through n optical SSMs. The modulated optical signal is combined by a WDM and split by a $1 \times m$ optical splitter. Then an $n \times m$ reflective-type MRR array is used to realize the optical true time delays for m beams. The reflective-type MRRs in each column have the same resonant wavelength, and contributed to the same beam. Finally, m PDs are employed to realize the optical-to-electrical conversion, and m antennas are used to emit the signals into the free space.

C. Optical Logic Operation

To meet the high demands for future optical computing and networking system, high-speed optical direct logic circuits with

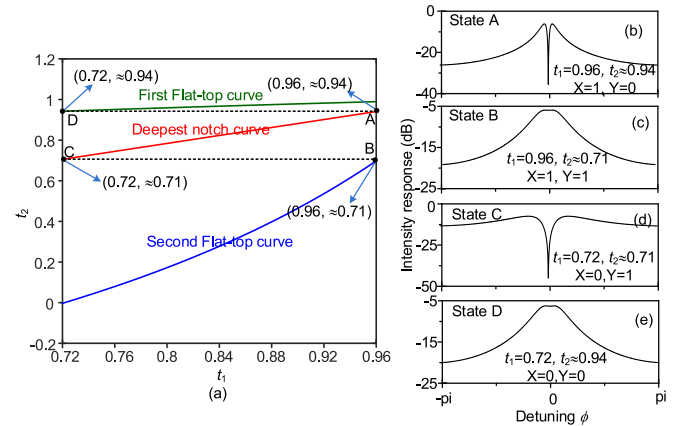


Fig. 17. (a) The calculated relationship for the two coupling coefficients for the two flat-top states and deepest notch states; (b-e) intensity responses at the Output Port under four different operating states which corresponds to four different combinations of the coupling coefficients.

parallel signal processing capacity, large-scale integration potential and small footprint are highly desired. Unlike optical logics realized based on optical nonlinearities [45], optical direct logics employ optical switches to implement the logic operations. The two inputs for logic operation are electrical pulses which are used to control the optical switches. An optical carrier is also required to probe the status of the optical switches out, so the output of the logic operation is in the form of light. If the input optical carrier is modulated by a microwave signal, optical switching of RF signals controlled by the logic operation is implemented, which would be particularly useful for future radio-over-fiber networks.

XOR and XNOR are two most useful logic gates, which, however, cannot be realized by a single MRR because the XOR and XNOR gates must have the “on” state under two different conditions and the “off” state under two other conditions controlled by the two logic inputs. Cascaded MRRs [46], [47] can solve this problem, but all the MRRs should be carefully pre-biased which significantly complicates the operation. Since the reflective-type MRR can achieve the “on” state (bandpass response) or the “off” state (notch response) under many combination of the upper and lower coupling coefficients, both the XOR and XNOR can be simply implemented using a single ring resonator.

According to Eq. (8), the flat-top optical filtering actually can be satisfied by two different t_2 for each t_1 if $at_1 > 1/\sqrt{2}$. Fig. 17(a) show the relationships between t_1 and t_2 to achieve different intensity responses, when a is still 0.98 and t_1 changes from 0.72 to 0.96. The deepest notch curve, obtained under the critical coupling (i.e., $t_2 = at_1$) condition, lies between the two flat-top curves. In order to realize optical logic gate, four pairs of coupling coefficients (denoted as A, B, C, D in Fig. 17(a)) are used, corresponding to four different states:

- State A ($t_1 = 0.96$ and $t_2 \approx 0.94$) is close to the critical coupling, so a deep notch can be obtained at the resonant wavelength, as shown in Fig. 17(b);
- State B ($t_1 = 0.96$ and $t_2 \approx 0.71$) is on the second flat-top curve, a flat-top response will be produced at the resonant wavelength, as shown in Fig. 17(c);

TABLE I
THE TRUTH TABLE OF THE PROPOSE LOGIC OPERATOR

X	Y	MRR state	XNOR result
1	0	bandstop	0
1	1	bandpass	1
0	1	bandpass	0
0	0	bandpass	1

- c) State C ($t_1 = 0.72$ and $t_2 \approx 0.71$) is on the deepest notch curve again, so a deep notch appears at the resonant wavelength, as depicted in Fig. 17(d);
- d) State D ($t_1 = 0.72$ and $t_2 \approx 0.94$) is on the first flat-top curve, so it is also a flat-top response at the resonant wavelength, as illustrated in Fig. 17(e);

Since the coupling coefficients is related to the voltages applied to the thermo-optic heater in the AMZIs, an optical operation can be achieved when two voltage sequences (denoted as X and Y) are applied to the heaters in the upper and lower AMZIs to make the coupling coefficients switch among the four operation states described above. Specifically, if the voltages applied to the lower and upper heaters are positively and negatively correlated with the coupling coefficients respectively, for State A the logic inputs X is at the high level and Y is at the low level (i.e., $X = 1, Y = 0$), the intensity response of the resonant wavelength is at the off state (logic 0); for State B, X and Y are both at the high level ($X = 1, Y = 1$), the intensity response of the resonant wavelength is at the on state (logic 1); for State C, X is at the low level and Y is at the high level ($X = 0, Y = 1$), the intensity response of the resonant wavelength is at the off state (logic 0); and for State D, X and Y are both at the low level ($X = 0, Y = 0$), the intensity response of the resonant wavelength is at the on state (logic 1).

The truth table of the proposed logic operation is summarized in Table I. From the truth table, we can see that the reflective-type MRR can perform the XNOR operation in the form of light at the output port. Since XOR operation is opposite to XNOR, it can be obtained with a similar approach if the applied voltages are both positively or negatively correlated to the coupling coefficient. This can be realized by setting the applied voltages both at the positive or negative modulation curve for the MZI thermo-optic modulation structures.

Fig. 18 shows the simulated results of the XNOR and XOR logic gates based on the reflective-type MRR. Two sequences of binary signal are applied to the lower and upper thermo-optic heaters of the reflective-type MRR with their voltages shown in Figs. 18(a) and 18(b). As can be seen from the output waveforms, which are shown in Figs. 18(c) and 18(d), XNOR and NOR operations are successfully realized. It is worth mentioning that tuning of the coupling coefficients will lead to a red shift of the resonant wavelength due to the thermal-optic effect, which affects the extinction ratio of the on and off states and causes the uneven voltage levels of pattern 1 and pattern 0. This problem might be solved by designing asymmetrical coupling in MZI couplers which has negligible red shift in resonant wavelengths when tuning the coupling coefficients [48].

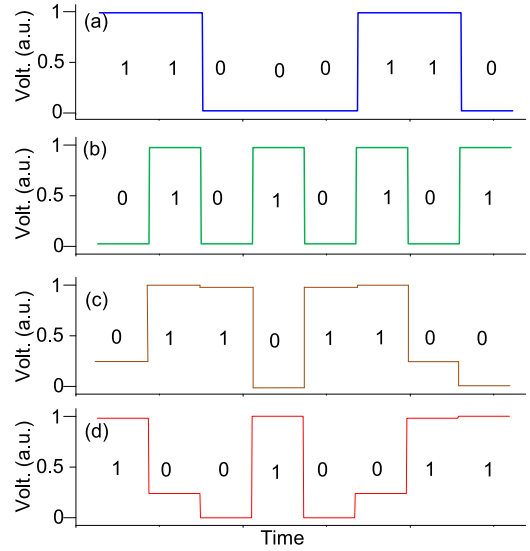


Fig. 18. Voltages applied to the heater in the (a) lower, (b) upper coupling regime and the calculated results of the (c) XNOR and (d) XOR operation.

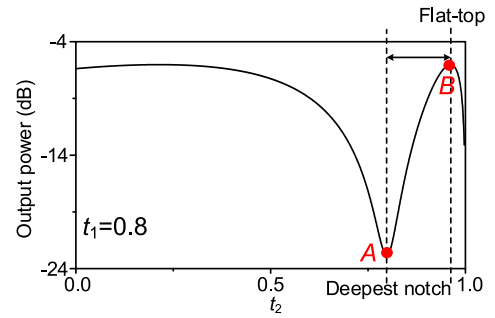


Fig. 19. The calculated output power as a function of t_2 when t_1 is fixed at 0.8.

Due to the limited modulation speed of the thermo-optic heater we used in the fabricated reflective-type MRR, the operation speed should be lower than 1 kbps. If other modulation schemes with high modulation speed, such as the carrier-injection modulation, the carrier-depletion modulation and the electric field effects are applied to the reflective-type MRR, higher operation speed will be possible [46], [47].

D. Electro-Optic Modulation

Since the intensity response of the reflective-type MRR can be switched between band-stop and bandpass, the optical power at the output port will be dynamically changed according to an electrical signal applied to the heaters on the MRR. If the reflective-type MRR is fabricated using an electro-optic crystal (for example, lithium niobate film), high speed electro-optic modulation would be achievable.

Fig. 19 shows the calculated optical power at the output port of the reflective-type MRR when t_1 is fixed at a constant value of 0.8 and t_2 is adjusted from 0 to 1. When t_2 is adjusted to match the critical coupling condition ($t_2 = 0.784$), the deepest

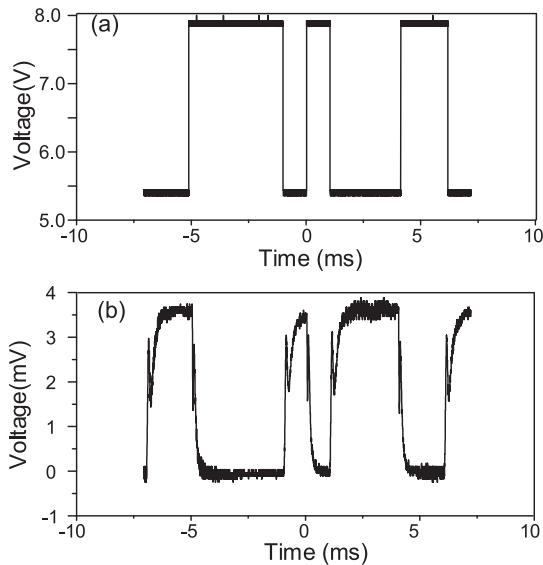


Fig. 20. Experiment result of the intensity modulation based on the reflective-type MRR. (a) The electrical signal applied to the heater and (b) the waveform of the modulated optical signal.

notch will be produced at the resonant wavelength, so the output power will reach the lowest value, which is marked as Point A in Fig. 19. When t_2 is increased to 0.959, the highest optical power will be output since a flat-top response is achieved, which is denoted as Point B in Fig. 19. The change of t_2 from the lowest to the highest points is only 0.175. Therefore, a relatively low drive voltage and a high modulation efficiency can be achieved.

A proof-of-concept experiment is performed, with the measured results shown in Fig. 20. Fig. 20(a) shows the electrical signal applied to the heater to change the coupling coefficient t_2 . The voltage levels set for pattern 1 and pattern 0 are 7.92 and 5.44 V, respectively. Fig. 20(b) illustrates the waveform of the optical output. As can be seen, electro-optic modulation is realized. It should be noted that the output waveform is reversed because in our fabricated reflective-type MRR, the increase of the voltage leads to the reduction of the coupling coefficient t_2 . There are spikes in the measured output of the modulator in Fig. 20 when the input voltage changes. It is due to the low tuning speed of the thermo-optic heaters in the coupling regimes of the reflective MRR, which can be reduced by using other kind of modulation mechanism [48]. The voltage difference between the minimum and the maximum transmission points, similar to the half-wave voltage of an MZM modulator, is 2.48 V, and the extinction ratio exceeds 16 dB. As a comparison, the half-wave voltage of the MZI thermo-optic modulator with 800 μm -long heater is about 18.75 V, so the drive voltage of the thermo-optic modulator based on the reflective-type MRR can be 1/7.56 of the conventional MZI thermo-optic modulator.

Since the proposed thermo-optic modulator is basically built on a ring resonator, wavelength drift induced by the input voltage is an inevitable issue. Fig. 21 shows the measured wavelength drift when adjusting the voltage to change t_2 . The

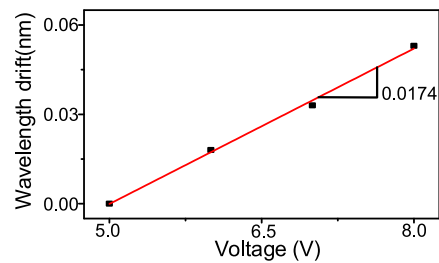


Fig. 21. Measured wavelength drift as a function of the voltage applied to adjust t_2 .

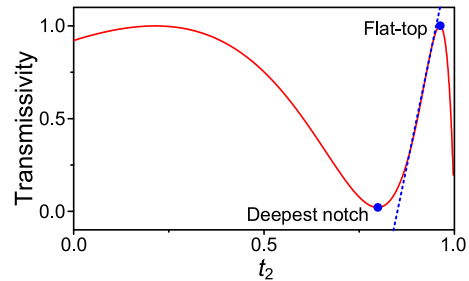


Fig. 22. The calculated normalized transmissivity of the reflective-type MRR functioning as an EOM.

wavelength drift rate is 0.0174 nm/V, which means that the wavelength drift for a modulator with an on-off voltage of 2.48 V is about 0.043 nm. Similar to the logic gate results shown in Part C, the bandwidth of such modulator is about several kHz, which is mainly limited by the modulation speed of the thermo-optic heater. To improve the modulation speed and to reduce the wavelength drift effect, some advanced modulation mechanism can be employed [49], [50].

It should be noted that if Fig. 19 is replotted using linear coordinate, as shown in Fig. 22, we can see that the linear modulation regime is large, making it suitable for microwave photonic applications.

IV. CONCLUSION

In this paper, we proposed and demonstrated several reconfigurable microwave photonic systems based on a reflective-type MRR to realize flat-top optical and microwave filtering, optical true time delay, optical XNOR/NOR logic operation, and electro-optic modulation. By placing a reflector at the drop port of an add-drop ring resonator, both the bandpass and band-stop responses can be obtained, which can realize flat-top optical and microwave filtering. In addition, by manipulating the slow-light and fast-light effects in the reflective-type MRR, a flat-top true time delay element is realized, which can be used to construct multi-beam PAAs. Furthermore, optic XNOR/NOR operations and electro-optic modulation can also be achieved based on a single reflective-type MRR. The reflective-type MRR features simple configuration, small footprint and high flexibility, which can overcome the deficiencies of conventional MRRs in terms of narrow signal processing bandwidth and poor reconfigurability and enable multifunctional microwave photonic systems on chip.

ACKNOWLEDGMENT

The authors would like to thank Zhizhi Yang and Liangzun Tang from the Key Laboratory of Radar Imaging and Microwave Photonics, Ministry of Education, Nanjing University of Aeronautics and Astronautics, Nanjing, China, for their assistance.

REFERENCES

- [1] D. G. Rabus and M. Hamacher, "MMI-coupled ring resonators in GaInAsP-InP," *IEEE Photon. Technol. Lett.*, vol. 13, no. 8, pp. 812–814, Aug. 2001.
- [2] A. Guarino, G. Poberaj, D. Rezzonico, R. Degl'Innocenti, and P. Günter, "Electro-optically tunable microring resonators in lithium niobate," *Nat. Photon.*, vol. 1, no. 7, pp. 407–410, 2007.
- [3] M. Zhang, C. Wang, R. Cheng, A. Shams-Ansari, and M. Lončar, "Monolithic ultra-high-Q lithium niobate microring resonator," *Optica*, vol. 4, no. 12, pp. 1536–1537, 2017.
- [4] S. Levy, M. Klebanov, and A. Zadok, "High-Q ring resonators directly written in As₂S₃ chalcogenide glass films," *Photon. Res.*, vol. 3, no. 3, pp. 63–67, 2015.
- [5] P. Absil *et al.*, "Wavelength conversion in GaAs micro-ring resonators," *Opt. Lett.*, vol. 25, no. 8, pp. 554–556, 2000.
- [6] W. Bogaerts *et al.*, "Silicon microring resonators," *Las. Photon. Rev.*, vol. 6, no. 1, pp. 47–73, 2012.
- [7] Q. Xu, D. Fattal, and R. G. Beausoleil, "Silicon microring resonators with 1.5- μ m radius," *Opt. Express*, vol. 16, no. 6, pp. 4309–4315, Mar. 2008.
- [8] A. Gondarenko, J. S. Levy, and M. Lipson, "High confinement micron-scale silicon nitride high Q ring resonator," *Opt. Express*, vol. 17, no. 14, pp. 11366–11370, 2009.
- [9] S. Wang *et al.*, "On-chip reconfigurable optical add-drop multiplexer for hybrid wavelength/mode-division-multiplexing systems," *Opt. Lett.*, vol. 42, no. 14, pp. 2802–2805, 2017.
- [10] F. Xia, L. Sekaric, and Y. Vlasov, "Ultracompact optical buffers on a silicon chip," *Nat. Photon.*, vol. 1, no. 1, pp. 65–71, 2007.
- [11] H. H. Zhu *et al.*, "High-sensitivity optical sensors based on cascaded reflective MZIs and microring resonators," *Opt. Express*, vol. 25, no. 23, pp. 28612–28618, 2017.
- [12] M. Sumetsky, R. Windeler, Y. Dulashko, and X. Fan, "Optical liquid ring resonator sensor," *Opt. Express*, vol. 15, no. 22, pp. 14376–14381, 2007.
- [13] A. Ksendzov and Y. Lin, "Integrated optics ring-resonator sensors for protein detection," *Opt. Lett.*, vol. 30, no. 24, pp. 3344–3346, 2005.
- [14] Q. Xu and M. Lipson, "All-optical logic based on silicon micro-ring resonators," *Opt. Express*, vol. 15, no. 3, pp. 924–929, 2007.
- [15] M. Kues *et al.*, "Passively mode-locked laser with an ultra-narrow spectral width," *Nat. Photon.*, vol. 11, no. 3, pp. 159–162, 2017.
- [16] A. Biberman, E. Timurdogan, W. A. Zortman, D. C. Trotter, and M. R. Watts, "Adiabatic microring modulators," *Opt. Express*, vol. 20, no. 28, pp. 29223–29236, 2012.
- [17] Q. Xu, S. Manipatruni, B. Schmidt, J. Shakya, and M. Lipson, "12.5 Gbit/s carrier-injection-based silicon micro-ring silicon modulators," *Opt. Express*, vol. 15, no. 2, pp. 430–436, 2007.
- [18] J. Capmany, I. Gasulla, and S. Sales, "Microwave photonics: Harnessing slow light," *Nat. Photon.*, vol. 5, no. 12, pp. 731–733, 2011.
- [19] J. Cardenas *et al.*, "Wide-bandwidth continuously tunable optical delay line using silicon microring resonators," *Opt. Express*, vol. 18, no. 25, pp. 26525–26534, 2010.
- [20] X. Xue *et al.*, "Mode-locked dark pulse kerr combs in normal-dispersion microresonators," *Nat. Photon.*, vol. 9, no. 9, pp. 594–600, 2015.
- [21] L. Chang *et al.*, "Ultra-efficient frequency comb generation in AlGaAs-on-insulator microresonators," 2019, *arXiv:1909.09778*.
- [22] T. J. Kippenberg, A. L. Gaeta, M. Lipson, and M. L. Gorodetsky, "Dissipative kerr solitons in optical microresonators," *Science*, vol. 361, no. 6402, Aug. 2018.
- [23] J. Liu *et al.*, "Nanophotonic soliton-based microwave synthesizers," 2019, *arXiv:1901.10372*.
- [24] E. Lucas *et al.*, "Ultralow-noise photonic microwave synthesis using a soliton microcomb-based transfer oscillator," *Nat. Commun.*, vol. 11, no. 374, 2020.
- [25] T. Hu *et al.*, "Thermally tunable filters based on third-order microring resonators for WDM applications," *IEEE Photon. Technol. Lett.*, vol. 24, no. 6, pp. 524–526, Mar. 2012.
- [26] J. R. Ong, R. Kumar and S. Mookherjee, "Ultra-high-contrast and tunable-bandwidth filter using cascaded high-order silicon microring filters," *IEEE Photon. Technol. Lett.*, vol. 25, no. 16, pp. 1543–1546, Apr. 2013.
- [27] P. A. Morton, J. Khurgin, Z. Mizrahi, and S. Morton, "Commercially packaged optical true-time-delay devices with record delays of wide bandwidth signals," in *Proc. CLEO: Appl. Technol.*, 2014, Paper AW3P.6.
- [28] A. Li and W. Bogaerts, "Using backscattering and backcoupling in silicon ring resonators as a new degree of design freedom," *Las. Photon. Rev.*, vol. 13, no. 6, 2019, Art. no. 1800244.
- [29] M. Huang, S. Li, M. Xue, L. Zhao, and S. Pan, "Flat-top optical resonance in a single-ring resonator based on manipulation of fast-and slow-light effects," *Opt. Express*, vol. 26, no. 18, pp. 23215–23220, 2018.
- [30] M. Huang, S. Li, Z. Yang, and S. Pan, "Analysis of a flat-top optical ring resonator," *Opt. Commun.*, vol. 451, pp. 290–295, 2019.
- [31] Q. Li, Z. Zhang, J. Wang, M. Qiu, and Y. Su, "Fast light in silicon ring resonator with resonance-splitting," *Opt. Express*, vol. 17, no. 2, pp. 933–940, 2009.
- [32] C. G. Roeloffzen *et al.*, "Low-loss Si₃N₄ TriPLeX optical waveguides: Technology and applications overview," *IEEE J. Sel. Topics Quantum Electron.*, vol. 24, no. 4, Jul./Aug. 2018, Art. no. 4400321.
- [33] X. Sun *et al.*, "Tunable silicon fabry-perot comb filters formed by sagnac loop mirrors," *Opt. Lett.*, vol. 38, no. 4, pp. 567–569, 2013.
- [34] B. E. Little, S. T. Chu, H. A. Haus, J. Foresi, and J.-P. Laine, "Microring resonator channel dropping filters," *J. Lightw. Technol.*, vol. 15, no. 6, pp. 998–1005, 1997.
- [35] J. Lloret *et al.*, "Tunable complex-valued multi-tap microwave photonic filter based on single silicon-on-insulator microring resonator," *Opt. Express*, vol. 19, no. 13, pp. 12402–12407, 2011.
- [36] Y. Long and J. Wang, "Ultra-high peak rejection notch microwave photonic filter using a single silicon microring resonator," *Opt. Express*, vol. 23, no. 14, pp. 17739–17750, 2015.
- [37] D. Zhang, X. Feng, and Y. Huang, "Simulation of 60-GHz microwave photonic filters based on serially coupled silicon microring resonators," *Chin. Opt. Lett.*, vol. 10, no. 2, 2012, Art. no. 021302.
- [38] Z. Tang, S. L. Pan, and J. P. Yao, "A high resolution optical vector network analyzer based on a wideband and wavelength-tunable optical single-sideband modulator," *Opt. Express*, vol. 20, no. 6, pp. 6555–6560, 2012.
- [39] S. L. Pan and M. Xue, "Ultrahigh-resolution optical vector analysis based on optical single-sideband modulation," *J. Lightw. Technol.*, vol. 35, no. 4, pp. 836–845, 2017.
- [40] M. Xue, S. F. Liu, and S. L. Pan, "High-resolution optical vector analysis based on symmetric double-sideband modulation," *IEEE Photon. Technol. Lett.*, vol. 30, no. 5, pp. 491–494, Mar. 2018.
- [41] T. Qing, S. P. Li, Z. Z. Tang, B. D. Gao, and S. L. Pan, "Optical vector analysis with attometer resolution, 90-dB dynamic range and THz bandwidth," *Nat. Commun.*, vol. 10, 2019, Art. no. 5135.
- [42] R. D. Esman *et al.*, "Fiber-optic prism true time-delay antenna feed," *IEEE Photon. Technol. Lett.*, vol. 5, no. 11, pp. 1347–1349, Nov. 1993.
- [43] L. Bliiek *et al.*, "Automatic delay tuning of a novel ring resonator-based photonic beamformer for a transmit phased array antenna," *J. Lightw. Technol.*, vol. 37, no. 19, pp. 4976–4984, 2019.
- [44] C. G. H. Roeloffzen *et al.*, "Silicon nitride microwave photonic circuits," *Opt. Express*, vol. 21, no. 19, pp. 22937–22961, 2013.
- [45] C. Zhao, X. Zhang, H. Liu, D. Liu, and D. Huang, "Tunable all-optical NOR gate at 10 Gb/s based on SOA fiber ring laser," *Opt. Express*, vol. 13, no. 8, pp. 2793–2798, 2005.
- [46] Q. Chen *et al.*, "1 Gbps directed optical decoder based on two cascaded microring resonators," *Opt. Lett.*, vol. 39, no. 14, pp. 4255–4258, 2014.
- [47] A. Godbole, P. Dali, V. Janyani, T. Tanabe, and G. Singh, "All optical scalable logic gates using Si₃N₄ microring resonators," *IEEE J. Sel. Topics. Quantum Electron.*, vol. 22, no. 6, pp. 326–333, Nov./Dec. 2016.
- [48] L. Zhao, S. Li, D. Ben, and S. Pan, "Tuning of transmission responses of an optical microring with negligible wavelength shift," *IEEE Photon. Technol. Lett.*, vol. 30, no. 3, pp. 227–230, Feb. 2018.
- [49] S. Feng, X. Luo, S. Du, and A. W. Poon, "Electro-optical tunable time delay and advance in a silicon feedback-microring resonator," *Opt. Lett.*, vol. 36, no. 7, pp. 1278–1280, 2011.
- [50] J. Ding *et al.*, "Ultra-low-power carrier-depletion Mach-Zehnder silicon optical modulator," *Opt. Express*, vol. 20, no. 7, pp. 7081–7087, 2012.

Shilong Pan (Senior Member, IEEE) received the B.S. and Ph.D. degrees in electronic engineering from Tsinghua University, Beijing, China, in 2004 and 2008, respectively. From 2008 to 2010, he was a “Vision 2010” Postdoctoral Research Fellow with the Microwave Photonics Research Laboratory, University of Ottawa, Canada. In 2010, he joined the College of Electronic and Information Engineering, Nanjing University of Aeronautics and Astronautics, China, where he is currently a Full Professor and an Executive Director of the Key Laboratory of Radar Imaging and Microwave Photonics, Ministry of Education. His research has focused on microwave photonics, which includes optical generation and processing of microwave signals, photonic microwave measurement, and integrated microwave photonics. He has authored or coauthored more than 430 research papers, including more than 240 papers in peer-reviewed journals, and 190 papers in conference proceedings. He is currently an Associate Editor for *Electronics Letters*, a Topical Editor for *Chinese Optics Letters*, and a Technical Committee Member of IEEE MTT-3 Microwave Photonics. He has also served as a Chair of a number of international conferences, symposia, and workshops, including the TPC Chair of the International Conference on Optical Communications and Networks in 2015, and a TPC Co-Chair of IEEE International Topical Meeting on Microwave Photonics in 2017. He is a Fellow of OSA, SPIE, and IET. He was selected as an IEEE Photonics Society Distinguished Lecturer in 2019.

Zhenzhou Tang (Student Member, IEEE) received the M.S. degree in information engineering and the Ph.D. degree in communication and information system from the Nanjing University of Aeronautics and Astronautics, Nanjing, China, in 2014 and 2019, respectively. He is also a Joint Ph.D. Student with the Photonics Research Group, Ghent University, Ghent, Belgium. His research interests are photonics-based microwave mixing, photonic integrated circuits, and radio over fiber communications. He has authored or coauthored more than 30 research papers, including more than 15 papers in peer-reviewed journals and 15 papers in conference proceedings. He is also one of the recipients of 2017 IEEE Photonics Society Graduate Student Fellowship.

Menghao Huang received the M.S. degree in electronic information science and technology in 2011 from the Nanjing University of Aeronautics and Astronautics, Nanjing, China, where he is currently working toward the Ph.D. degree with the Key Laboratory of Radar Imaging and Microwave Photonics, Ministry of Education. His research interests are silicon photonics, analog photonic link.

Simin Li (Member, IEEE) received the B.S. and Ph.D. degrees from Nanjing University, Nanjing, China, in 2009 and 2014, respectively. In 2014, she joined the Key Laboratory of Radar Imaging and Microwave Photonics, Ministry of Education, where she is currently a Lecturer. Her current research interests focus on integrated microwave photonic device and system.